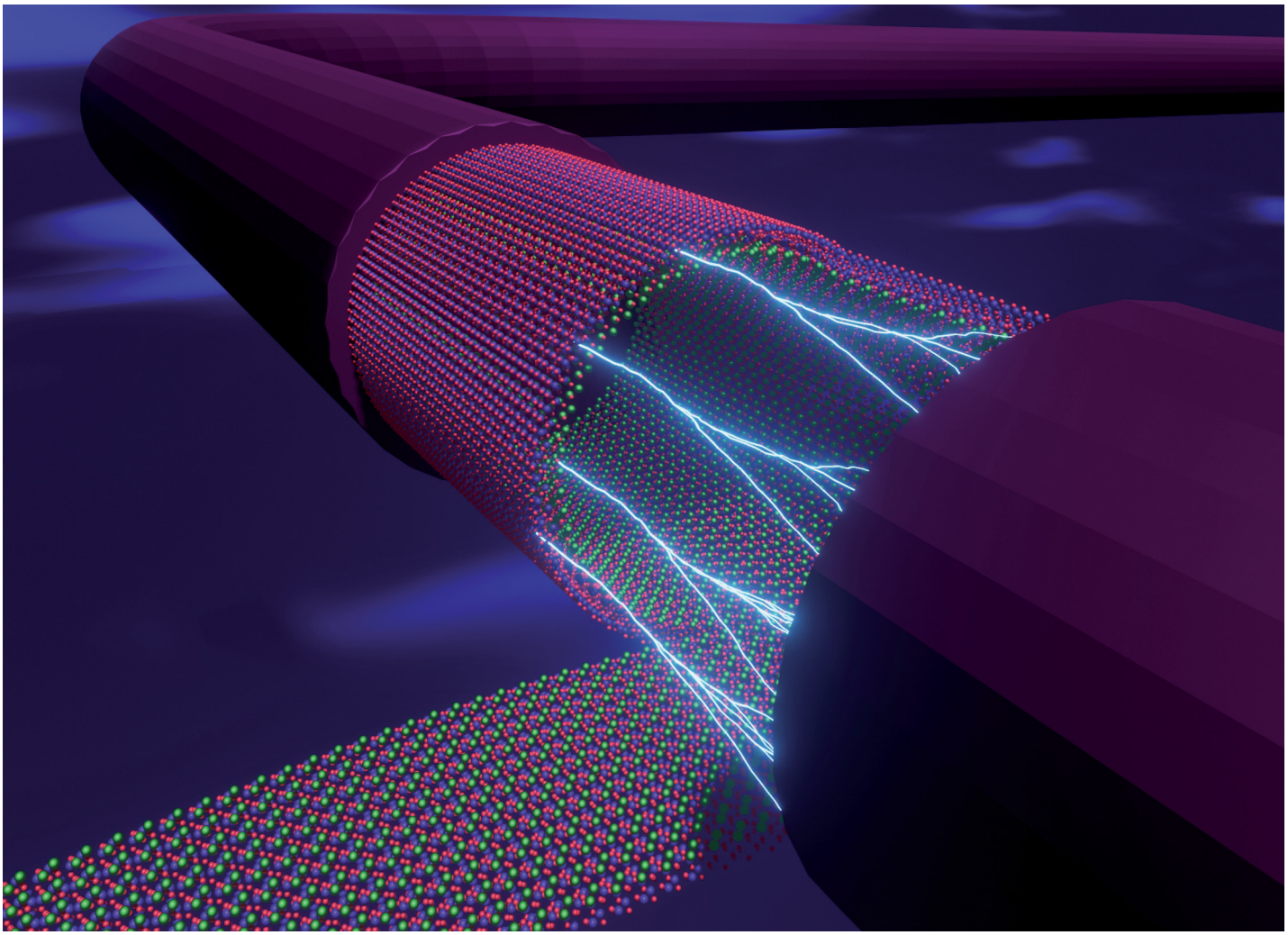

Research performed at Prof. L. Panchakarlas' laboratory at IIT, Bombay, India in collaboration with Dr R. Arenal's group at INMA, CSIC-Universidad de Zaragoza and Laboratorio de Microscopías Avanzadas, Universidad de Zaragoza, Spain.

Strontium-deficient Sr_xCoO_2–CoO_2 nanotubes as a high ampacity and high conductivity material

Miniaturization of electronics demands interconnectors with high ampacity and conductivity, which conventional conductors cannot offer. Our strategy converts a quasi-1D into a 2D crystal structure that rolled into tubular structures, producing a large quantity of Sr-deficient misfit $SrCoO_2$–CoO_2 nanotubes, shows the highest reported ampacity value in any inorganic oxide-based material and the highest breakdown power per unit channel length among regular interconnect materials. These nanotubes are potential building blocks for high-power electronic applications.

As featured in:

See Raul Arenal *et al.*, *Mater. Horiz.*, 2022, **9**, 2115.

ROYAL SOCIETY OF CHEMISTRY

rsc.li/materials-horizons

Registered charity number: 207890

Materials Horizons

ROYAL SOCIETY OF CHEMISTRY

COMMUNICATION

View Article Online
View Journal | View Issue

Cite this: *Mater. Horiz.*, 2022, 9, 2115

Received 9th December 2021, Accepted 13th May 2022

DOI: 10.1039/d1mh01987b

rsc.li/materials-horizons

Strontium-deficient Sr_xCoO_2–CoO_2 nanotubes as a high ampacity and high conductivity material†

Kankona Singha Roy,[a] Simon Hettler,[bc] Raul Arenal[*bcd] and Leela S. Panchakarla‡[a]

Continuous miniaturization of electronics demands the development of interconnectors with high ampacity and high conductivity, which conventional conductors such as copper and gold cannot offer. Here we report the synthesis of Sr-deficient misfit Sr_xCoO_2–CoO_2 nanotubes by a novel crystal conversion method and investigate their electrical properties. Bulk $Sr_6Co_5O_{15}$ having a quasi-one-dimensional CoO_6 polyhedral structure (face-sharing octahedron and trigonal prismatic CoO_6 arranged in one-dimension) is converted to Sr_xCoO_2–CoO_2 nanotubes where CoO_2 adopts a two-dimensional edge-sharing CoO_2 layered structure in a basic hydrothermal process. Electrical properties measured on individual nanotubes demonstrate that these nanotubes are semiconducting with a conductivity of 1.28×10^4 S cm^{-1} and an ampacity of 10^9 A cm^{-2}, which is the highest reported ampacity value to date of any inorganic oxide-based material. The nanotubes also show a breakdown power per unit channel length (P/L) of $\sim$38.3 W cm^{-1}, the highest among the regularly used interconnect materials. The above results demonstrate that Sr_xCoO_2–CoO_2 nanotubes are potential building blocks for high-power electronic applications.

New concepts

To date, the literature reports the synthesis of low dimensional materials from high to low dimensional, *e.g.* from 3D to 2D/1D materials. In this work, we report crystal structure conversion from quasi-one dimensional to 2D in misfit strontium cobalt oxide for the first time. Upon achieving the two-dimensional crystal structure, it further rolls into tubular structures due to existing misfit strain and stabilizes the metastable structure. Further investigation of the metastable 1D nanotube demonstrates a unique crystal structure representing edge-sharing CoO_2 layers intercalated by a unit of CoO_x and $SrCoO_2$, which has not been reported earlier. Along with this, we have also explored the electrical properties of these nanotubes at the individual nanotube level. These nanotubes show a conductivity value of 1.28×10^4 S cm^{-1}, even higher than that of CNTs and an ampacity of 10^9 A cm^{-2}, which is the highest reported ampacity value to date of any inorganic oxide-based material. These nanotubes also exhibit a breakdown power per unit channel length (P/L) of 38.3 W cm^{-1}, the highest among the regularly used interconnect materials suggesting that these materials could be building blocks for high-power electronic applications. We believe the synthetic strategy developed in this work opens up possibilities to produce many metastable compounds.

1. Introduction

Intercalated layered cobalt oxides have shown rich physical phenomena and drawn significant attention due to their eccentric electrical, thermal, and magnetic properties.[1,2] These intercalated layered cobalt oxides have been applied as cathodes in rechargeable batteries.[3,4] They show high Seebeck coefficients regardless of their metallicity, which will be applicable for thermoelectric devices.[2,5,6] When these CoO_2 layers are decoupled (by intercalating with water, $Na_{0.3}CoO_2{\cdot}1.3H_2O$), they exhibit unconventional superconductivity.[7] CoO_2 and other transition metal dichalcogenide layers intercalated with two-dimensional layers with different lattice parameters (the so-called misfit layered compounds (MLC)) have generated some interest lately.[8,9] CoO_2 layers are proposed to show ferroelectric instabilities when intercalates are progressively removed. However, making intercalated CoO_2 nanotubes (NTs) is found to be synthetically challenging. Recently, the synthesis of $CaCoO_2$/$SrCoO_2$ intercalated misfit CoO_2 nanotubes was demonstrated starting from bulk misfit $Ca_3Co_4O_9$ or $Sr_3Co_4O_9$.[10,11] The band gap of these nanotubes is found to be dependent on the type of intercalate, being 1.9 eV in $CaCoO_2$–CoO_2 and 1.2 eV in $SrCoO_2$–CoO_2.[10,11] However, the yield of $CaCoO_2$–CoO_2 nanotubes is found to be low, and the

[a] *Department of Chemistry, Indian Institute of Technology Bombay, Powai, Mumbai, 400076, India*
[b] *Instituto de Nanociencia y Materiales de Aragon (INMA), CSIC-Universidad de Zaragoza, Calle Pedro Cerbuna 12, 50009 Zaragoza, Spain. E-mail: arenal@unizar.es*
[c] *Laboratorio de Microscopias Avanzadas (LMA), Universidad de Zaragoza, Calle Mariano Esquillor, 50018 Zaragoza, Spain*
[d] *ARAID Foundation, 50018 Zaragoza, Spain*

† Electronic supplementary information (ESI) available. See DOI: https://doi.org/10.1039/d1mh01987b

‡ This author is deceased, 24th December 2021.

yield of $SrCoO_2$–CoO_2 nanotubes depends on the ability to synthesize bulk metastable $Sr_3Co_4O_9$. Moreover, the electrical properties of these nanotubes have not been studied yet, which demands further research on improved synthesis methods and investigation of the properties of these materials.

Here, we report, a rather unique crystal conversion process to make metastable Sr_xCoO_2–CoO_2 nanotubes. The quasi-one-dimensional crystal structure of bulk $Sr_6Co_5O_{15}$ is treated under basic hydrothermal conditions to form Sr_xCoO_2–CoO_2 nanotubes (SCO-NTs, $x < 1$), which are Sr-deficient compared to the previously studied misfit $SrCoO_2$–CoO_2 NTs.[11] The nanotubular phase of Sr-deficient Sr_xCoO_2–CoO_2 has been indicated as SCO-NTs throughout the manuscript for simplification. Commonly, inorganic nanotubes are synthesized directly from pure elements or from the corresponding bulk structure,[9] which is in contrast to our approach as the SCO-NT structure is different from that of the parent bulk. X-ray photoelectron spectroscopy (XPS), high resolution (scanning) transmission electron microscopy (HR(S)TEM) imaging, selected area electron diffraction (SAED) along with energy-dispersive X-ray spectroscopy (EDS) and electron energy-loss spectroscopy (EELS) measurements were conducted to identify the structure and the chemical composition of these nanotubes.

Also, we have explicitly studied both the physical and the electrical properties of SCO-NTs at the individual nanotube level by patterning them *via* electron beam lithography. The as-synthesized SCO-NTs can sustain a breakdown current-carrying capacity (J) of as high as 0.88×10^8 A cm^{-2} (without contact resistance correction) and 2.49×10^9 A cm^{-2} (contact resistance corrected) for a single NT, which is a few orders of magnitude higher than those of the conventional interconnect metals (Cu, Al, Au, *etc.*)[12–23] and van der Waals materials[24–27] and even comparable to that of multi-wall carbon nanotubes (MWCNTs) (1.23×10^8 A cm^{-2}).[28–30] Compared to the state-of-the-art materials, *e.g.*, graphene,[31,32] MWCNTs,[33] and single-wall (SW)CNTs,[33–35] SCO-NTs show higher conductivity (σ) on the order of 1.28×10^4 S cm^{-1}, which is one order of magnitude higher than that of SWNTs and graphene. Besides, SCO-NTs exhibited a high breakdown power per unit channel length (P/L) $\sim$ 38.3 W cm^{-1}, which is the highest among all of the regularly used interconnect materials and close to the highest reported value for boron nitride coated-SWNTs ($\sim$45 W cm^{-1}).[36] This value indicates the electrical robustness of these materials under a high voltage sweep. These high values of current carrying capacity with high conductivity open a window for these materials to be used as a very promising interconnect candidate.

2. Results and discussion

2.1 Structural characterization of Sr_xCoO_2–CoO_2 (SCO-NTs)

SCO-NTs have been achieved upon reaction with $Sr_6Co_5O_{15}$ (see crystal structure in Fig. 1 and X-ray diffraction analysis in Fig. S1 in the ESI†) under basic hydrothermal conditions at 220 °C for 12 h. SEM images show a high yield of nanotubes (Fig. 2(a) and (b)) with the presence of some 2D flakes and unreacted bulk material (Fig. S2 in ESI†). These NTs have external diameters of 10–70 nm and lengths ranging from 600 nm to 4 μm. Several high-resolution (HR)(S)TEM images on different nanotubes are presented in Fig. 2(c)–(e) and Fig. S3 and S4 in the ESI,† which clearly show that the nanotube is crystalline with several defects and imperfections. The area of the acquired HRTEM image is marked by the green square in the inset TEM image of Fig. 2(e). The line profile taken along the blue line (Fig. 2(e)) shows that this nanotube contains two types of d-spacings along the c-axis, one with $\sim$0.89 nm and another with $\sim$0.54 nm. The former spacing corresponds to $SrCoO_2$ intercalate between the CoO_2 layers matching with the existing $SrCoO_2$–CoO_2 misfit phase.[11] The latter spacing does not agree with the d-spacing of pure metastable CoO_2 (0.45 nm). However, it can be linked to the distance between two successive CoO_2 layers, a Sr-deficient misfit phase, possibly intercalated partially with Na ions coming from the basic medium reaction conditions. This d-spacing was observed in low amounts in pure $SrCoO_2$–CoO_2 misfit NTs and was declared as a stacking fault.[11] In the following, we refer to this phase as intercalated CoO_2 layers. Fig. 2(c) shows an HR-STEM image of another SCO-NT with a well-ordered stack of complete misfit layers and intercalated CoO_2 layers indicated by black and red lines, respectively. Distortion in the outer boundary has also been observed in some NTs with both misfit and intercalation phases (Fig. 2(d)). Fig. S4 in the ESI† further presents HRTEM images for different nanotubes with various wall thicknesses. The relative amounts of misfit $SrCoO_2$–CoO_2 and intercalated CoO_2 phases differ considerably between NTs as can be seen from these additional images in Fig. S4 (ESI†).

To gain more insight into the crystal structure, we collected and analyzed selected area electron diffraction (SAED) patterns of individual nanotubes (Fig. 2(f)). In the SAED pattern, all the spots with similar interplanar spacing are marked with dashed circles. The measured d-spacings with corresponding Miller indices are annotated, and the original diffraction pattern without annotations is also given in Fig. S5 in the ESI† for reference. The green double arrow in the SAED pattern marks the tubular axis. Along the c-axis, a periodicity of 0.9 nm is observed, with a strong {003}, a weak {002} and a broad {001} pattern suggesting the existence of a superstructure of alternating CoO_2 and $SrCoO_2$ layers. Known from the misfit NTs,[11] there are eight spots of {110} and {220} reflections of $SrCoO_2$ on the red marked circles with d-spacings of 0.36 and 0.18 nm, respectively. These planes have a multiplicity factor of four, implying two types of $SrCoO_2$ sheets in the same nanotube, which are rotated by 30° with respect to each other. There are twelve pairs of CoO_2 reflections of {200} and {020} (indicated with blue dashed circles) with d-spacings of 0.25 and 0.14 nm, respectively. These planes have a multiplicity factor of six, implying two types of CoO_2 sheets in the same nanotube, which are rotated by $\sim$20°. Most investigated NTs showed two sets of sheets but NTs with a single set or multiple sets of sheets were found. The spots of both subsystems are spread by equal angles (4°); thus, the layers' chiral angle is 2°, which is equivalent to

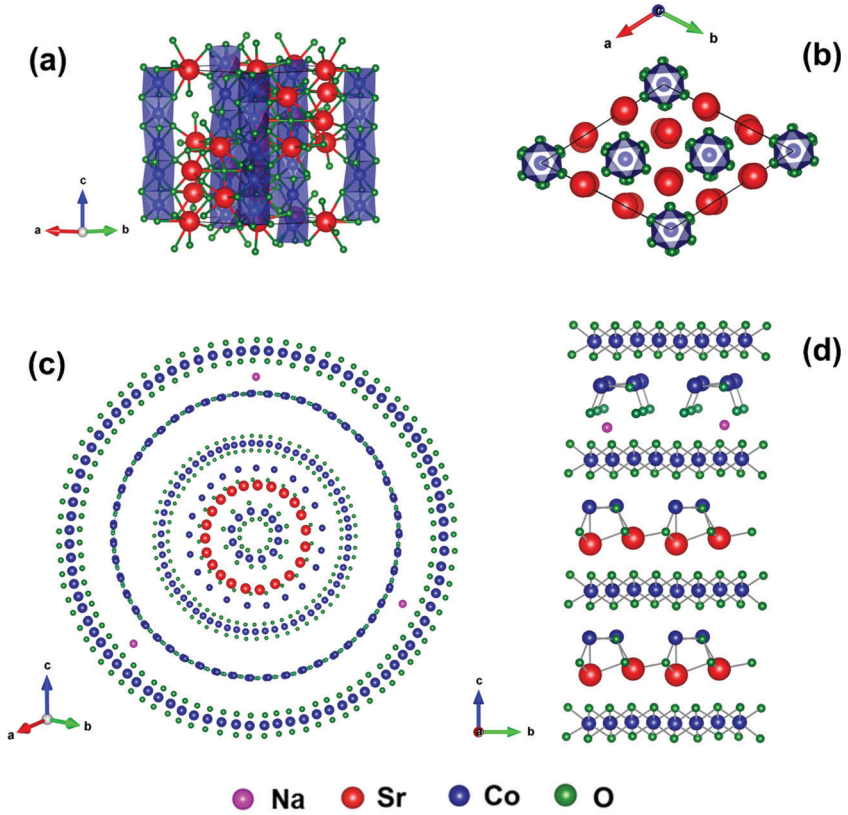

Fig. 1 (a) and (b) Crystal structures of $Sr_6Co_5O_{15}$ bulk through the *c*-axis and *ab*-plane, respectively. Crystal structures of the proposed Sr-deficient SCO-NTs with intercalated CoO_2 layers: (c) along the cross-sectional direction, and (d) along the *a*-axis.

half of the azimuthal spreading of the spots. The lattice parameters of CoO_2 and $SrCoO_2$ in the *a*-direction are commensurate. Thus, the two sets of spots, which are marked by green dashed ellipses (Fig. 2(f)) and are related to the reflections of the {200} planes with a *d*-spacing of 0.25 nm, come from both the CoO_2 and the $SrCoO_2$ layers. There are two sets of spots with a *d*-spacing of 0.27 nm, marked by red circles in Fig. 2(f) corresponding to {020} reflections of $SrCoO_2$. Thus, SAED confirmed that SCO nanotubes have a composite crystal structure of primary CoO_2 layers between $SrCoO_2$ layers in the misfit structure.

Fig. S6 in the ESI† presents the elemental composition analysis of the NTs by STEM-EDS. Fig. S6(a)–(d), ESI† show examples of the EDS spectra, where the main contributions of O, Co and Sr and Na are clearly visible. Fig. S6e, ESI† shows the mean, minimum and maximum atomic percentages of O, Co, Sr and Na found in the analysis of several NTs. The average composition is 73.2% O, 16% Co, 7.1% Sr, and 3.8% Na with two exemplary spectra presented in Fig. S6(a)–(d), ESI.† The atomic percentage of Sr compared to Co is considerably lower than expected for a pure misfit $SrCoO_2$–CoO_2 phase (14%), confirming that the NTs primarily consist of CoO_2 layers. A variation of the elemental composition within a single NT could not be detected. The Co and Sr contents are found to vary considerably between different NTs, while the sum of both elements (Co + Sr) is rather constant (Fig. S6e, ESI†). This shows that the relative amounts of Na-stabilized CoO_2 and CoO_2 stabilized between $SrCoO_2$ layers in the misfit structure differ between NTs.

X-Ray photoelectron spectroscopy (XPS) analysis was performed to determine the chemical environment and oxidation state of cobalt in SCO-NT. Fig. S7a in the ESI† indicates the wide spectra of the NT where the binding energy peaks located at 131.8 eV, 780.2 eV and 531.9 eV correspond to Sr 3d, Co 2p and O 1s, respectively. A high-resolution scan for Co 2p shows two peaks corresponding to $2p_{3/2}$ and $2p_{1/2}$ centered at 779.8 eV and 794.8 eV and a satellite peak at 790 eV, respectively (Fig. S7b in ESI†). It has been reported that the satellite peak at 790 eV confirms the presence of Co^{3+}.[37] In the case of $LiCoO_2$ and delithiated Li_xCoO_2, it has been shown that the broadening of the satellite peak (*i.e.*, full width at half maximum) and its relative area help in understanding the cobalt oxidation state and the amount of lithium present (*x*).[37] Therefore, assuming a similar dependency for Sr-based CoO_2, we fitted the peaks for Co 2p, and the full width at half maximum (FWHM) for the satellite peak (790 eV) is found to be 3.1 eV with a relative area of 5.2%. This observation suggests partial oxidation of Co^{3+} to Co^{4+}. Deconvolution of Co $2p_{3/2}$ peaks indicates the presence of three peaks centered at 780 eV, 781.3 eV and 782.8 eV, which can be assigned to the contribution of Co^{3+} (area 62.07%), multiplets of Co^{3+}/Co^{4+} (area 30.9%) and Co^{4+} (area 7.03%), respectively (Fig. S7c in ESI†). The Co atoms seem to be present

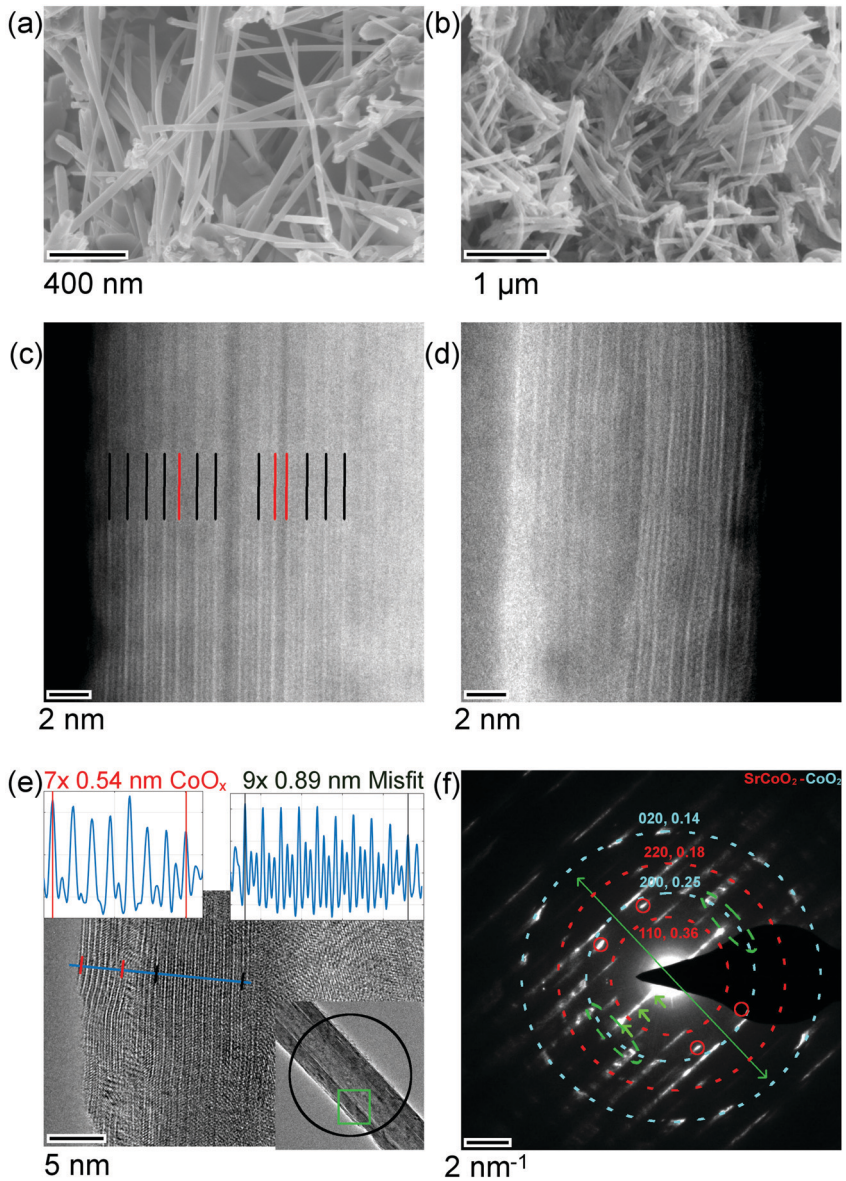

Fig. 2 (a) and (b) SEM images of SCO-NTs. (c) HRSTEM image of an SCO-NT with a well-ordered stack of complete SCO misfit layers and intercalated CoO_2 layers indicated by black and red lines. (d) HRSTEM image of a NT with a rather disordered outer border, where both misfit and intercalation phases can be seen. (e) TEM analysis of an SCO-NT: HRTEM image and corresponding line profiles show two *d*-spacings at the NT border, which are attributed to intercalated CoO_2 (0.54 nm) and the SCO misfit structure (0.89 nm). Inset shows a low magnification TEM image of the nanotube, where the area of the HRTEM image is marked with a green square and the corresponding area selected for diffraction (SAED pattern in (f)) is marked by a black circle. (f) SAED pattern of the nanotube. A long green double-sided arrow indicates the tubular axis and small green arrows indicate basal reflections. Dashed circles denote spots corresponding to the same interplanar spacings, and measured values are given together with the associated Miller indices. The $SrCoO_2$ and CoO_2 subsystems are represented by red and light blue, respectively. The original diffraction pattern without annotations is given in Fig. S5 in the ESI† for reference.

primarily in the 3+ oxidation state, which agrees well with the reported literature.[37] The Co 3p core XPS spectrum is recorded to understand further the oxidation process of Co^{3+} (Fig. S7d in ESI†). The splitting of Co 3p into Co $3p_{3/2}$ and Co $3p_{1/2}$ is not observed because of the minimal binding energy difference/spin–orbit coupling constant. The satellite peak located at 70.6 eV has a FWHM of 4.1 eV with a 9.1% relative area, strongly suggesting the oxidation of Co^{3+}, and is in good accordance with the reported literature for cobaltates.[37] It is known that the core 3s peaks are very sensitive to the metal spin state for transition metals.[37] To understand the spin state (low spin or high spin), we further recorded the Co 3s XPS spectrum (Fig. S7e in ESI†). Fig. S7e in the ESI† shows a main peak at 102.4 eV and a very weak satellite peak in the binding energy region of 109–115 eV. The FWHM of the main peak is found to be 3.6 eV, which suggests a low spin configuration (d^5) of Co^{4+}, supporting the findings in the literature. This clearly supports the (partial) oxidation of Co^{3+} to Co^{4+} in our Sr-deficient misfit

nanotubes. Also, Na 1S XPS gives a prominent peak at 1070.3 eV, which proves the presence of Na ions as intercalates between CoO_2 layers (Fig. S7f, ESI†). Furthermore, we have deconvoluted O 1s peaks into three peaks located at 529.9 eV, 531.5 eV and 533.2 eV, which can be assigned to the contribution from lattice oxygen (area 47.55%), adsorbed surface hydroxyls/strontium carbonate on the surface (area 46.44%) and adsorbed H_2O on surface (area 6.01%) species, respectively (Fig. S7g in ESI†), based on the reported literature.[38–41] Detailed analysis of Co $2p_{3/2}$ and O 1s for SCO-NT is presented in Table S1(a) and (b) (ESI†).

Fig. S8 in the ESI† shows the O-K and Co-L edges obtained by TEM-EELS measurements on individual NTs. The near-edge fine structures (ELNES) of EELS for the O-K edge show a sharp peak at 530 eV followed by a valley and a broader excitation between 535 and 546 eV. This spectrum closely resembles the EELS signal obtained on pure misfit SCO-NTs,[11] but differs considerably from the published spectra of CoO, where the Co ions are found in the Co^{2+} configuration and do not show a peak at 530 eV.[42,43] As the intensity at 530 eV increases with increasing Co oxidation state, such as in Co_3O_4, the presented data with a strong peak at 530 eV suggest an even higher oxidation state of Co^{3+} or higher. This is confirmed by the Co-L edge ELNES analyses, which reveal a Co-L_3 peak at a rather high energy of 781 eV as previous studies show that a higher valence leads to a shift to higher energies of the Co-L_3 edge.[42] In summary, the EELS results on Co-L and O-K edges suggest that Co is found in an oxidation state of Co^{3+} or even higher, which supports our analysis from Co XPS spectra. Spatially-resolved (SR) EELS analysis of an NT with both misfit and intercalated CoO_2 phases is shown in Fig. S9 (ESI†). The data indicate that indeed the Sr content is reduced in the intercalated phase compared to the misfit phase confirming previous results from imaging and diffraction. Small changes in the ELNES of the O-K and the Co-L edges suggest a minor difference of valences between the two phases.

In addition, we performed optical measurements on the SCO-NTs. The work function of these NTs is calculated from the ultraviolet photoelectron spectroscopy (UPS) as explained in the literature[44] (Fig. S10 in ESI†) and it is found to be 6.1 eV. We measured the UV-Vis absorbance spectra of the SCO-NTs (Fig. S11 in ESI†). It is observed that they show a major absorption peak around 432 nm. The band gap is calculated from the Tauc plot and it is found to be 0.6 eV.

2.2 Growth mechanism

In order to understand the growth mechanism of these nanostructures, nanotubes at different reaction times have been analyzed. The SEM images of NTs obtained at 6 h in Fig. 3(a) and (b) reveal the growth point of the nanotubes as marked by red arrows, and yellow arrows indicate grown SCO-NTs from those growth points. The TEM image in Fig. 3(c) clearly shows the growth of the nanotubes from the bulk and Fig. 3(d) indicates the low contrast regions (marked in yellow arrows) in the bulk, identified as the growth point (as seen in Fig. S12 in the ESI†).

Fig. S13 in the ESI† shows a study of the growth mechanism by a comparison of the reaction product after 0 h (parent bulk),

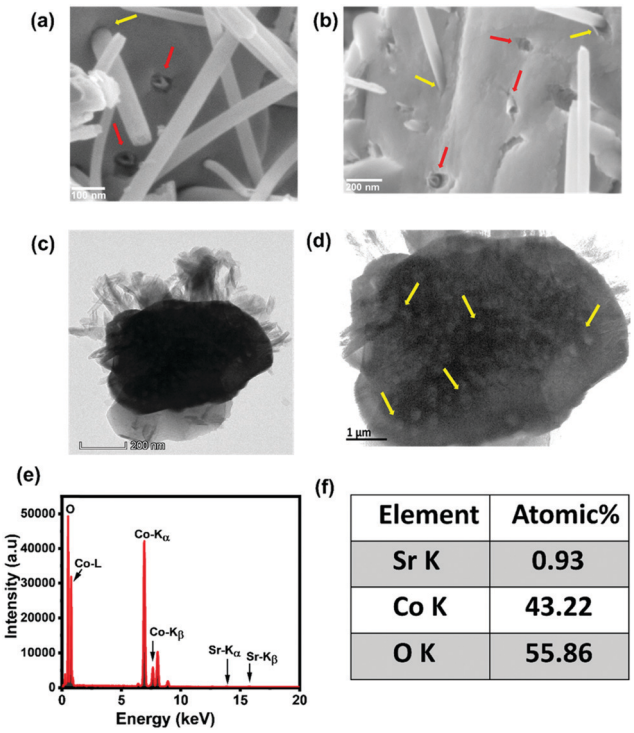

Element	Atomic%
Sr K	0.93
Co K	43.22
O K	55.86

Fig. 3 (a) and (b) SEM images of the sample obtained at 6 h (during growth of the nanotubes), where red arrows indicate where nanotubes are about to grow and the routes of the grown nanotubes are marked with yellow arrows. TEM images show (c) the nanotubes growing out of the bulk (strontium-deficient Sr_xCoO_2–CoO_2), and (d) the low contrast regions act as growth points for nanotubes. (e) EDS spectrum of the area presented in (d) and the relative atomic percentages of Sr, Co, and O are shown in (f).

1 h, 3 h and 10 h of reaction time. The rod-like morphology of the parent bulk is maintained after 1 h, where partial exfoliation is visible on the surface of the Sr-leached bulk. Small NTs start to appear after 3 h of reaction time, which continue growing during the prolonged reaction time until almost the complete bulk material is consumed after 10 h.

$Sr_6Co_5O_{15}$ consists of infinite columns of face-sharing trigonal prismatic and octahedra of CoO_6 polyhedra that propagate along the crystallographic *c*-direction, separated by SrO_8 units (Fig. 1 and Fig. S1 in ESI†).[45] The distance between two adjacent cobalt cations in the face-sharing CoO_6 polyhedra is similar or slightly lower than the distance between two neutral Co atoms in the metal.[45] Thus, the face-sharing configuration requires high energy due to the increased electrostatic repulsion between the two closely spaced high valent Co ions. Upon basic hydrothermal treatment, most of the Sr dissolves in basic solutions as proven by the EDX analysis (Fig. 3(e) and (f)), which reveals a very low Sr content in the remaining bulk and growing nanotubes (average of 0.7–1.3 atomic% of Sr). This leaves the face-sharing one dimensional (1D) CoO_6 polyhedral chains unstable, which convert to edge-sharing CoO_6 sheets. Due to misfit stress between the SrCoO–CoO_2 layers and dangling bonds at the sheet's edges, these sheets crystalize into tubular form and these nanotubes may be seen as coming

out of the bulk (Fig. 3 and Fig. S12 in ESI†). CoO_2 could also be partially intercalated with Na ions that are present in the solution. One-dimensional growth could result from increased volume, while converting face-sharing CoO_6 to edge-sharing CoO_6 *via* oxygen insertion and screw dislocation.

2.3 Electrical properties of SCO-NT devices

The electrical properties of SCO-NTs are studied by fabricating four and two-terminal devices with NTs as the channel/active material on a Si/SiO_2 substrate, with 285 nm SiO_2 as the gate dielectric. Fig. 4 shows the schematic representations and SEM images of two- and four-probe devices. Fig. 5(a) demonstrates the typical resistance *vs.* temperature (*R vs. T*) plot under a vacuum of a four-terminal device for an SCO-NT with a length of 2.2 μm and a diameter of 57 nm. The device with equidistant probes, being 405 nm apart, is shown in the inset of Fig. 5(a). The resistance decreases exponentially from low temperature (10 K) to 170 K showing that the nanotubes are semiconducting. The resistance saturates and slightly increases up to 300 K. At room temperature, the resistance (R) is found to be ~2900 Ohm giving a conductivity value of 1.28×10^4 S cm^{-1}. It was proposed that for 1D layered nanotubes, not the entire cross-sectional area does take part in conduction, but only a few outer layers (attached to the electrode) participate in the current transport.[46] Thus, the conductivity value reported here could be a lower estimate. We also measured the resistance at room temperature for a prolonged period of time showing that the resistance is stable for a time period of 400 s (Fig. S14 in ESI†). From lower to higher voltage, the *I–V* graph becomes linear to non-linear (Fig. S15 in ESI†), suggesting that the conduction shifts from ohmic-conduction to trap-filling conduction/defect-mediated conduction. These observations indicate that SCO-NTs can follow space-charge limited current (SCLC) theory for conduction.[47]

In the case of two-probe measurements (device setup as in Fig. 4(a) and (b)), the voltage applied to the NTs was gradually increased, and the current flow along the NTs was measured.

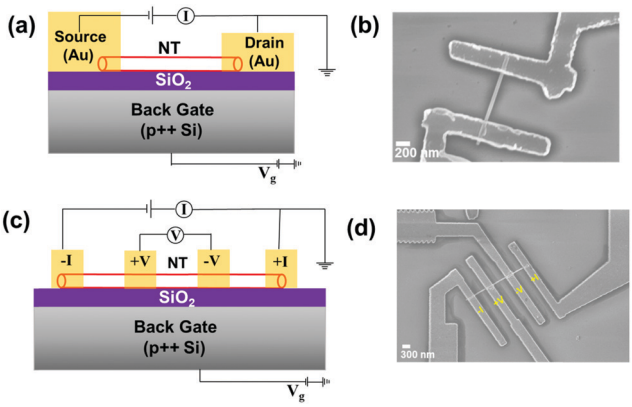

Fig. 4 (a) Schematic representation of a typical two-probe device of SCO-NT FET showing the source, drain and back-gate electrode. (b) SEM image of a two-probe device. (c) Schematic representation of a four-probe device of SCO-NT, where current is sourced from outer electrodes and inner electrodes sensed the voltage drop. (d) SEM image of a four-probe device.

In total, we have measured *I–V* curves for around 30 devices in a two-probe configuration with tube diameters ranging from 10 to 50 nm (see Fig. S16 in ESI†). The output and transfer characteristics of one of these devices can be seen in Fig. 5(b) and (c), respectively, measured under ambient conditions at room temperature for a channel length of 176 nm and a diameter of 13.5 nm. Fig. S17 in the ESI† represents the output and transfer characteristics of a typical two-probe device for a channel length of 185 nm and a diameter of 16.2 nm. It is necessary to mention here that gate leakage current has also been monitored throughout all the measurements, as seen from Fig. 4.

The drain current (I_d) for a typical two-terminal nanotube device could not be altered significantly by applying a gate voltage (V_g) as high as 50 V (Fig. 5(b)). This suggests that the nanotubes might be of semi-metallic nature where the mobile charge carriers are not considerably affected by the applied gate voltage (V_g). In Fig. 5(c), the V_g is swept from −50 V to +50 V for a fixed V_d of 3 V. Both Fig. 5(b) and (c) reveal that the nanotubes are of p-type semiconducting nature (slight increment in the current at negative V_g).

From the linear regime of the transfer characteristics graph (Fig. 5(c)), we can extract the linear field-effect mobility using the following equation: $\mu = \frac{L^2}{C_{ox} V_d} \times \frac{dI_d}{dV_g}$ where, L = the length of the NT, V_d = the drain voltage and C_{ox} = the gate to channel capacitance. $C_{ox} = 2\pi\varepsilon \in_0 L/\ln(2h/r)$ is calculated with $\varepsilon \sim 3.6$ the average dielectric constant of SiO_2, h = 285 nm the thickness of the SiO_2 substrate and r = the radius of the nanotube, which gives a value of $\mu = 0.9 \pm 0.2$ cm^2 V^{-1} S^{-1}. We measured several devices and the mobility of the NT varies from 0.6 to 0.9 cm^2 V^{-1} S^{-1}. Several effects influence this value making it only a lower estimate. As it has been obtained from two-probe measurements, contact resistance can significantly decrease the obtained mobility value. To calculate the contact resistance, we use the following equation: $R = R_{NT} + 2R_c$ where, R = the total resistance from the two-probe measurement, R_{NT} = the resistance of the nanotube and R_c = the contact resistance.[48,49] Several four-probe measurements (Fig. 5(a), and Fig. S14 in ESI†) reveal that the nanotube resistance is in the order of 3000–4000 Ohm at room temperature. Considering these values, the contact resistance varies from 15 kOhm to 28 kOhm, which is almost 5–7 times higher than the nanotube resistance. The high contact resistance therefore strongly affects the measured curves (Fig. 5(b)–(d)) and the determined mobility value. Moreover, the fact that the current does not saturate with increasing voltage, leading to device breakdown, further decreases these mobility values. Also, the samples were spin-coated from solution for the contacting process, in which solvent residues and moisture can be trapped between the layers acting as a scattering center and could further decrease the determined mobility.[50] Further studies are required to explicitly eliminate these effects in order to have more accurate values. Considering μ = 0.9 cm^2 V^{-1} S^{-1}, we calculated the carrier concentration following the equation $\sigma = ne\mu$, where, σ = the conductivity, n = the carrier concentration, e = the

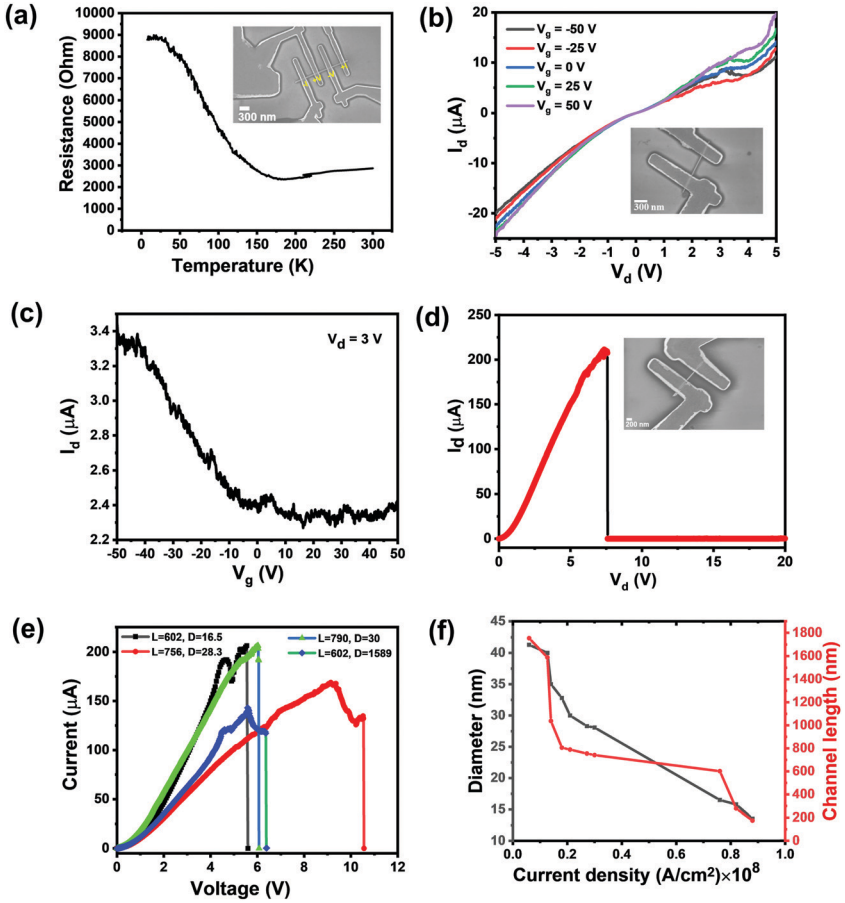

Fig. 5 (a) Resistance *vs.* temperature (T) plot for a four-probe device (SEM image of the device is shown as an inset). Output (b) and transfer (c) characteristics of a two probe SCO-NT FET (SEM image of the device is shown in the inset of (b)). (d) I_d–V_d graph up to breakdown for the two-probe device shown in the inset. (e) I_d–V_d graphs up to breakdown for four different two probe devices with different channel lengths (L) and diameters (D). Maximum current density with respect to NT diameter and the device channel length is represented in (f).

electronic charge and μ = the mobility, which gives a value of $n \sim 10^{22}$ cm^{-3}.

We have performed temperature-dependent I–V characteristics for typical two-probe devices. The consistent increase in resistance with decreasing temperature confirms the assumption of a semiconducting behavior for these NTs (Fig. S18a in ESI†). A plot of logarithmic current with drain voltage shows that the current is measured starting from a small voltage (50 mV), which indicates that, despite the large contact resistance, the contact is of ohmic nature and the NTs possess a minimal barrier height for current flow (Fig. S18b in ESI†). The ohmic nature at low voltages is as well evident in Fig. S15a (ESI†). Moreover, the dopant activation energy (E_a) can be calculated from the Arrhenius equation as follows: $\sigma \propto e^{\left(-E_a/K_bT\right)}$, where K_b is the Boltzmann constant.[47,50] The activation energy (E_a) is calculated to be 0.1 meV considering the fact that contact resistance has a negligible effect on the activation energy, as reported previously (Fig. S18c in ESI†).[47,51] The activation energy is very small compared to the thermal energy $K_bT \sim 25$ meV at room temperature. This implies a very high charge carrier concentration for these NTs, which is in agreement with the calculated carrier concentration (n) at room temperature. These values indicate that SCO-NTs act as a highly intrinsically doped semiconductor. In order to determine the nature and origin of the dopant thoroughly for these NTs, further experimental and theoretical studies are needed, which is beyond the scope of the present work.

We will now focus on the current-carrying capacities of the SCO-NT devices. The maximum current depends primarily on three parameters such as connector geometry, electrical resistance and temperature rise.[52] Among them, the effect of connector geometry is uncomplicated and easily achievable. In contrast, the electrical resistance is a quantity that depends on many interconnected factors. Similarly, many parameters affect the material's thermal conductivity, affecting the maximum allowed temperature rise. SCO-NTs have a resistivity of 8.8 × 10^{-5} Ohm cm. This low resistivity can be attributed to the high charge carrier concentration and the small band gap (0.6 eV from Fig. S11 in ESI†). A single nanotube of length 670 nm and diameter 13.5 nm can withstand a 208 μA current under ambient conditions before breakdown (at zero gate voltage)

(Fig. 5(d)), and this gives a current density of 0.88×10^8 A cm^{-2} (without R_c correction), which outperforms conventionally used metal (Cu, Al, Au *etc.*) interconnects.[20,53–57] This value of high current density is comparable to the highest reported value for WS_2 NTs[38] (2.4×10^8 A cm^{-2}) as inorganic nanotubes (INTs) and even close to the reported value for MWCNTs (1.23×10^8 A cm^{-2}).[28,29] Elimination of the contact resistance gives a value of 2.49×10^9 A cm^{-2}, which is almost similar to the reported value for SWCNTs (3.4×10^9 A cm^{-2}).[28,35] Our findings of maximum current density could be a lower estimation as the devices do not reach saturation with applying bias. The SCO-NT devices can endure a high voltage (V_d) until the failure point, even higher than that of CNTs.[30] The sharp decrease in the current in Fig. 5(d) indicates the failure/breakdown of the NT. It is known that, due to effective Joule heating, the resistance for all the NTs shoots up just before the point of breakdown, which might decompose the sample.[58]

More than 30 devices, in addition to the more than 30 for the two-probe configuration, have been studied with various diameters and channel lengths to understand the influence of both parameters on the maximum current carrying capacity (Fig. 5(e) and Fig. S16 in ESI†). Fig. 5(e) demonstrates that the nanotubes can carry a maximum of 150–210 μA current depending on the diameter and channel length giving a current density ranging from 0.14×10^8–0.88×10^8 A cm^{-2}. The dependence of the current-carrying capacity on the nanotube diameter and channel length is shown in Fig. 5(f). Like CNTs, the maximum current density decreases with increasing diameter and channel length.[29] The best value is observed for an NT with a diameter of 13.5 nm and a channel length of 176 nm. The reason behind this can be explained by the Joule heating associated with current conduction. It is well understood that the heat generated needs to be dissipated to reach a high current density. It has already been reported that inner shells show a higher temperature increase for any applied voltage than the outer shells.[29] Thus, in the case of NTs with a bigger diameter, outer shells can dissipate the heat faster than the inner shells, thus making the inner shells more susceptible to a temperature high enough to result in a breakdown of the device. Similarly, devices with smaller channel lengths can carry high current as hot phonons can readily decay into metal contacts. A device with a longer channel length (poor Joule heat dissipation as the contacts are far apart) is thus prone to easy breakdown with lower current carrying capacity.

SEM imaging was performed after the breakdown of the device to understand the breakdown process. Fig. S19 in the ESI† shows that the failure took place along the nanotubes and not inside the metal contacts, as pointed out by the yellow arrow. In order to analyze the mechanism of electrical breakdown, we used the power-law dependence, *i.e.*, $J \propto \rho^{-m}$, where $m = 0.5$ for the breakdown triggered by the ideal Joule heating and $m > 0.5$ for the defect-induced electromigration and ρ = the resistivity of the NT.[26] Fig. S20 in the ESI† shows the plot of $\log J$ *vs.* $\log \rho$ with the fit of the power-law equation with $m = 0.64$. This value suggests that the breakdown in these devices does not follow the ideal Joule heating. The breakdown could be due to defect-induced electromigration coupled with Joule heating before the tube decomposes. As seen from Fig. S19 in the ESI,† the failure is more likely to occur near the cathode (neither at the center nor near the anode), which could be due to electrical stress. This can be explained as follows: when the current flows from the cathode to the anode, electron-wind force (F) is applied close to the cathode, causing the atomic displacement (electromigration) and hence the breakdown. Under ambient conditions, moisture and oxygen-related species can easily get adsorbed on the surface of the NT. So, the breakdown is influenced by electromigration as the formation of defects, vacancies and diffusion at the surface escalate the rate of electromigration. This electromigration could be suppressed under vacuum measurements or capping by any dielectric layer. Likewise, we observed an increase in current under a vacuum ($\sim 10^{-5}$ Torr) compared to ambient conditions, which supports our assumption (Fig. S21 in ESI†). Under a vacuum, the surface-adsorbed moieties are largely removed, resulting in better contact, leading to lower electromigration.

The fabrication of the contact lids by the deposition technique might affect the measurement results in several ways.[56] To diminish the effects, a minimal dose and low acceleration voltage has been used for locating the nanotube and imaging the device after fabrication. On the other hand, the high current used in the deposition process of contact lids might damage the Si/SiO_2 substrate.

To verify that the current measured in a two-probe configuration (till device breakdown) originates from the nanotubes and not from the Si/SiO_2 (285 nm) substrate, an I–V curve between two unconnected metal pads was measured using the methods as discussed before. However, the current we observed was in the pA range, suggesting no leakage through the substrate (Fig. S22 in ESI†). Besides, these devices are stable for over ten months under ambient pressure and temperature, as no current degradation was observed in the I–V curves (Fig. S23 in ESI†), which indicates a high NT stability and promises a hassle-free real-life application as an interconnect.

Fig. 6(a) shows a comparison plot of ampacity vs conductivity for metals and nanocarbons and nanocarbon composites.[12–23,28–35,53–57,59–62] SCO-NTs are found to be one of the best materials next to the best reported CNT-Cu composite[55] and c-Al NW[56] showing a higher ampacity at slightly reduced conductivity. Considering the fact that achieving high ampacity and conductivity in the same material is challenging, SCO-NTs hold a potential chance to replace the existing interconnects (metals) in the future. Comparing the current carrying capacity with other existing materials shows that SCO-NT materials hold a possible chance as an interconnect (Fig. 6(b)).[24–27,36,50,63–65] SCO-NT devices show a current density (J) of 0.88×10^8 A cm^{-2} under ambient conditions (without R_c correction), which is higher than most of the reported inorganic materials (SnO_2,[24] WTe_2,[26] $TaSe_3$,[27] $ZrTe_3$[25] *etc.*) by a few orders of magnitude and close to the best reported WS_2 NTs (2.4×10^8 A cm^{-2})[50] and Te-boron nitride (BN) NTs (1.5×10^8 A cm^{-2})[24] among all inorganic materials. Eliminating

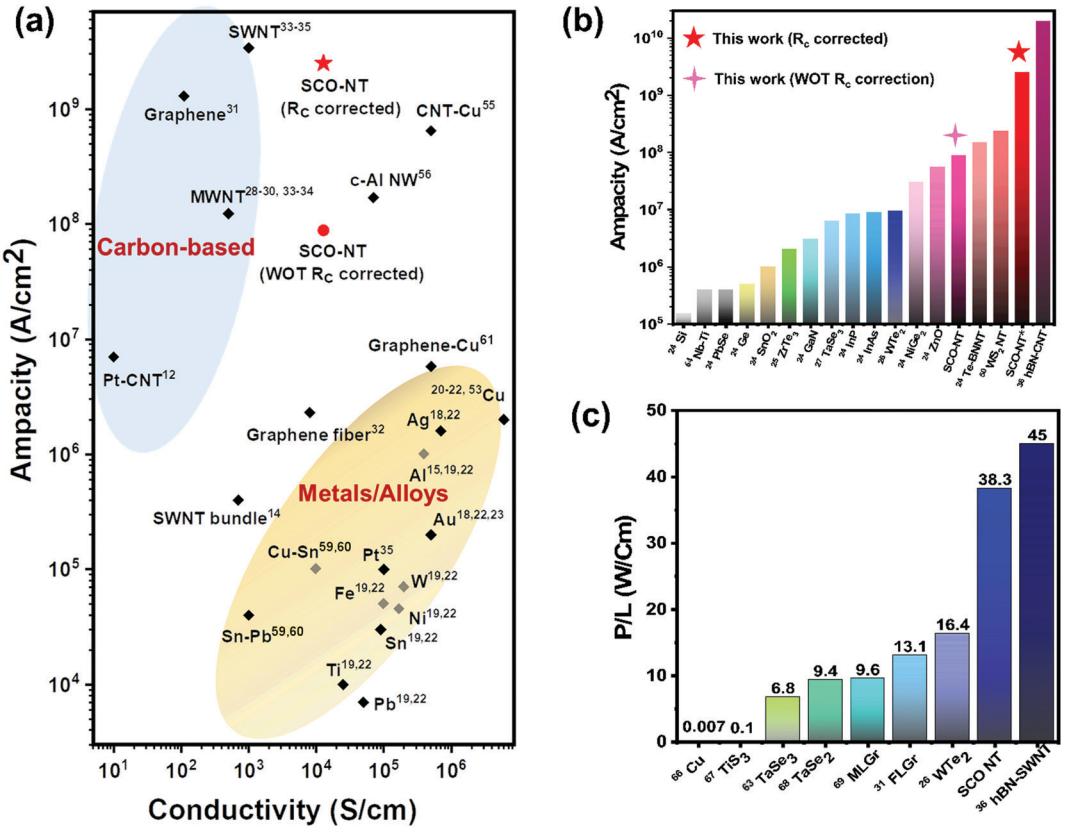

Fig. 6 (a) Ashby plot of ampacity vs conductivity for several materials such as metals (*e.g.* Cu, Au, Ag, Al, *etc.*), alloys (*e.g.* Sn–Pb), nanocarbons (*e.g.* single-walled (SW)NTs, graphene) and composites (*e.g.* carbon NT-Cu) including SCO-NTs. SCO-NTs (without eliminating contact resistance) exceed the ampacity of metals/nanocarbons and with contact resistance elimination SCO-NTs could have an ampacity as high as that of SWNTs with higher conductivity than SWNTs. (b) Comparison of the ampacity of SCO-NTs (with/without contact resistance) with other inorganic-based semiconductor nanowires/nanotubes (NWs/NTs). (c) Averaged maximum input power per channel length (*P*/*L*) for different channel materials that can endure under air.

the contact resistance indicates an even higher current density of 2.49×10^9 A cm^{-2}, which is immediately next to the highest reported single-walled (SW) BNNTs (2×10^{10} A cm^{-2})[36] and close to SWCNTs on SiO_2 (3.4×10^9 A cm^{-2}).[28,35,36] The results suggest that improving the device architecture and contacts can even further increase the current density. In Fig. 6(c), we compared the maximum electrical power per unit channel length (*P*/*L*) that these nanotubes can withstand just before the breakdown to understand the reliability of NTs under high bias.[26,31,36,63,66–69] Remarkably, SCO-NTs can endure the highest *P*/*L* ~ 38.3 W cm^{-1} (not R_c corrected), which surpasses many of the interconnect candidates such as CVD-grown multilayer graphene (MLGr) ~ 9.6 W cm^{-1},[69] mechanically exfoliated few layer graphene (FLGr) ~ 13.1 W cm^{-1},[31] and polycrystalline Cu ~ 0.007 W cm^{-1},[66] and stand next to the best reported BN-SWNT ~ 45 W cm^{-1}.[36] It is worth mentioning that polycrystalline Cu experiences high grain boundary electromigration resulting in an easy breakdown and low *P*/*L* value. The high value of *P*/*L* for SCO-NTs could be because of the electrical robustness of these nanotubes under electrical stress. Overall, in this work, we present the electrical properties of SCO-NTs with a high current carrying capacity along with good electrical conductivity and high electrical breakdown power per unit channel length. With the current findings of this work, we believe that the use of any capping layer (*e.g.* Al_2O_3, h-BN *etc.*), high thermal conducting substrate (*e.g.* sapphire) and measurements under a vacuum could significantly improve the device performance, which requires further experiments in detail.

3. Conclusions

We have developed a strategy to synthesize Sr_xCoO_2–CoO_2 nanotubes (SCO-NTs) with high yields. A quasi-one-dimensional crystal structure, *i.e.*, $Sr_6Co_5O_{15}$, is converted from face-sharing polyhedra (from 1D crystal structure) to edge-sharing octahedra (2D layered crystal structure). In the obtained nanotubes, CoO_2 layers are stabilized in combination with the $SrCoO_2$ layer (making a misfit unit) and additionally intercalated in between these misfit units, possibly with the aid of Na ions, yielding a structure predominantly made of CoO_2 layers. HR(S)TEM, SAED, EDS, EELS and XPS studies on these nanotubes distinctly proved the presence of CoO_2 layers, both in the misfit units with $SrCoO_2$ and in the intercalated form. The growth of these nanotubes has been spotted to emerge

from the SCO bulk, revealing the growth mechanism based on a crystal conversion process, unlike the usual rolling mechanism.

SCO-NTs act as highly intrinsically doped semiconductors showing a high current-carrying capacity ($\sim 10^9$ A cm^{-2}) along with high conductivity (1.28×10^4 S cm^{-1}) and high electrical breakdown power per unit channel length (~ 38.3 W cm^{-1}). These electrical properties suggest that SCO-NTs are likely to be a promising candidate as an interconnect, fulfilling the requirements suggested by ITRS. We believe that the device performance could be improved further by using a high thermal conducting substrate capping layer (*e.g.*, Al_2O_3, hBN *etc.*), shorter device channel length (<100 nm) and applications under vacuum, which requires further experiments in detail. Nevertheless, we expect that with constant improvement of the synthesis/fabrication techniques, these SCO-NTs may emerge as a highly interesting research topic on their own.

4. Experimental section

4.1 Synthesis of bulk $Sr_6Co_5O_{15}$ (SCO bulk)

Bulk $Sr_6Co_5O_{15}$ was synthesized by dissolving strontium nitrate tetrahydrate [$Sr(NO_3)_2{\cdot}4H_2O$] and cobalt nitrate hexahydrate [$Co(NO_3)_2{\cdot}6H_2O$] in a 6 : 5 ratio in Milli Q water. The salt solution was concentrated by heating at 70 °C for an hour, which is then transferred to an alumina boat. The alumina boat was then kept inside a tube furnace, which was preheated at 900 °C. The boat was held at 900 °C for 6 h. After completion of the reaction, the tube furnace was allowed to cool down to room temperature naturally.

4.2 Synthesis and analysis of Sr_xCoO_2–CoO_2 nanotubes (SCO-NTs)

In a typical synthesis of the core–shell nanotubular phase, $Sr_6Co_5O_{15}$ bulk (20 mg) was sonicated in a 2.5 M NaOH solution for 15 min and transferred into an air-tight autoclave. The autoclave was kept in a constant temperature oven and heated to 220 °C at a ramp rate of 5 °C min^{-1}. The autoclave was maintained at that temperature for 12 h and cooled to room temperature overnight. The product was washed several times with Milli-Q water until it became neutral (pH = 7) and dried in an oven by keeping at 60 °C overnight. The dried powder (SCO-NTs) was used for all the characterization. In order to understand the nanotube formation (growth mechanism), a similar experiment starting with $Sr_6Co_5O_{15}$ in basic hydrothermal conditions is designed for a reaction time of 6 h instead of 12 h.

4.3 Characterization techniques

Multiple characterization techniques were used to study the structure and composition of the synthesized material at the individual nanotube level, including scanning electron microscopy (SEM) (ZEISS GeminiSEM 560), transmission electron microscopy (TEM) with scanning ((S)TEM) (Thermo Scientific, Themis 300 G3) and coupled with energy-dispersive X-ray spectroscopy (EDS) (Super-X detector). HR(S)TEM analysis was conducted using two aberration-corrected Titan microscopes (Thermo Fisher Scientific). HRTEM, SAED and TEM-EELS studies (Gatan Image Filter (GIF) Tridiem, acceptance angle 11.9 mrad) were performed with an image-corrected microscope operated at 300 kV. A probe-corrected microscope equipped with a high-brightness field-emission gun operated at 300 kV was used for acquisition of HRSTEM images with a high-angle annular dark-field detector (convergence/acceptance angle 25/48 mrad), EDX spectra with an Oxford Instruments Ultim Max TLE 100 detector and SR-EELS using a GIF tridiem ESR 866 EEL spectrometer. SR-EELS studies were performed at 80 kV and an acceptance angle of 68 mrad.

The phase of the powder was confirmed by X-ray diffraction (XRD) using a PANalytical (Netherlands) diffractometer system (model Empyrean) with CuK_α radiation (λ = 1.54 Å). Chemical state analysis and ultraviolet photoelectron spectroscopy (UPS) were conducted using an X-ray photoelectron spectroscopy (XPS) instrument (Kratos Analytical, AXIS Supra). All the XPS spectra are calibrated using contaminated C 1s spectra with the peak at 284.8 eV, and the peak fitting is done using a nonlinear Shirley background and with a least-square fitting method using a Gaussian × Lorentzian (70% × 30%). We have used an Agilent Technologies (model: carry 100 UV-Vis) UV-Vis spectrophotometer for recording UV-Vis spectra.

4.4 Device fabrication and measurements

Firstly, NT powder was dispersed in *iso*-propyl alcohol (IPA) (HPLC grade) and sonicated for 1 min. The suspension was spin-coated at 3000 rpm for 1 min on a pre-patterned highly p-doped Si/SiO_2 wafer. SEM was used to mark and map the individual nanotubes. Nanotubes of length 1–4 μm with a 15–50 nm diameter were selected for the SCO-NT fabrication process. E-beam resist EL9 and PMMA 950K 2% were spin-coated on the substrate with nanotubes before e-beam exposure. Source/drain electrodes were patterned by electron beam lithography (Raith 150 two). For development, the substrate was dipped into a 1 : 3 MIBK/IPA mixture for 30 s and then immediately immersed into IPA for 10 s. The work function of the nanotubes is found to be 6.1 eV by UPS measurements (Fig. S4 in ESI†). Metal contacts of Cr/Pt/Au (2 nm/50 nm/50 nm) were deposited by sputtering (an Orion sputter) followed by Ar bias cleaning to ensure that the remaining PMMA on the contact pattern is removed, where Pt (6.35 eV) acts as the work function material (enabling ohmic contact). Cr was used because of its excellent adhesion property, which makes the lift-off process easier. For the final step, *i.e.*, lift-off process, the metal-deposited substrate was kept in acetone for 5 h and then washed with acetone, IPA and then dried under a N_2 gun. Four terminal devices were also fabricated following the same procedure. The two probe devices were measured with a probe station connected to a semiconductor characterization system (Proxima Keysight B1500A) at room temperature under ambient conditions. The four-probe devices were measured with a physical property measurement system (PPMS, Quantum Design). For a four-probe geometry, the current (I) injected from the outer two probes, and the voltage developed between the inner two probes are measured continuously for various

temperatures. To investigate the temperature-dependence of the *I–V* curve for these NTs, the as fabricated devices were mounted in a vacuum cryostat (Lakeshore, CRX-4K) and the current-*vs*.-voltage (*I–V*) characteristics were governed as a function of temperature. The ampacity measurements are performed at ambient temperature and pressure. To ensure that the imaging and subsequent metal deposition do not create current pathways on the substrate surface by creeping or hopping, we designed a test structure using the same fabrication procedure on a nanotube-free area of the substrate and the measurements have been carried out similarly like earlier.

Conflicts of interest

The authors declare no conflicts of interest.

Acknowledgements

This paper is dedicated to the memory of Professor Leela S. Panchakarla, dear supervisor (K.S.R) and colleague, outstanding scientist, who died prematurely. Dear late Prof. L.S.P. would like to acknowledge Science and Engineering Research Board under the Department of Science and Technology (DST-SERB), Government of India for funding (EMR/2016/003594). K.S.R. acknowledges the Department of Chemistry, Department of Physics and Department of Materials Engineering and Materials Science, Indian Institute of Technology (IIT) Bombay and Industrial Research and Consultancy Center (IRCC), Sophisticated Analytical Instrument Facility (SAIF), Centre of Excellence in Nanoelectronics (CEN) IIT Bombay and Fund for Improvement of S&T Infrastructure (FIST) for all the facilities provided. K.S.R. sincerely thanks Gayatri Vaidya at IIT Bombay for helpful assistance and discussion about the fabrication process. S.H. and R.A. acknowledge funding from the European Union's Horizon 2020 research and innovation programme under the Marie Sklodowska-Curie grant agreement no. 889546 and from the Spanish MICINN (project grant PID2019-104739GB-100/AEI/10.13039/501100011033). R. A. acknowledges funding from the Government of Aragon (project DGA E13-20R) and European Union H2020 program "ESTEEM3" (823717). Some of the TEM measurements were performed in the Laboratorio de Microscopias Avanzadas (LMA) at the Universidad de Zaragoza (Spain).

References

1 A. Semenova, D. Kellerman and A. Markov, *ECS Trans.*, 2010, **25**, 155–162, DOI: **10.1149/1.3334803**.
2 T. Motohashi, Y. Sugimoto, Y. Masubuchi, T. Sasagawa, W. Koshibae, T. Tohyama, H. Yamauchi and S. Kikkawa, *Phys. Rev. B: Condens. Matter Mater. Phys.*, 2011, **83**, 195128, DOI: **10.1103/PhysRevB.83.195128**.
3 B. V. Rami Reddy, R. Ravikumar, C. Nithya and S. Gopukumar, *J. Mater. Chem. A*, 2015, **3**, 18059–18063, DOI: **10.1039/C5TA03173G**.
4 L. Wu, W. H. Lee and J. Zhang, *Mater. Today: Proc.*, 2014, **1**, 82–93, DOI: **10.1016/j.matpr.2014.09.017**.
5 M. M. Mallick and S. Vitta, *Inorg. Chem.*, 2017, **56**, 5827–5838, DOI: **10.1021/acs.inorgchem.7b00476**.
6 D. J. Singh and D. Kasinathan, *J. Electron. Mater.*, 2007, **36**, 736–739, DOI: **10.1007/s11664-007-0154-0**.
7 K. Takada, H. Sakurai, E. Takayama-Muromachi, F. Izumi, R. A. Dilanian and T. Sasaki, *Nature*, 2003, **422**, 53–55, DOI: **10.1038/nature01450**.
8 R. T. Leriche, A. Palacio-Morales, M. Campetella, C. Tresca, S. Sasaki, C. Brun, F. Debontridder, P. David, I. Arfaoui, O. Šofranko, T. Samuely, G. Kremer, C. Monney, T. Jaouen, L. Cario, M. Calandra and T. Cren, *Adv. Funct. Mater.*, 2021, **31**, 2007706, DOI: **10.1002/adfm.202007706**.
9 M. Serra, R. Arenal and R. Tenne, *Nanoscale*, 2019, **11**, 8073–8090, DOI: **10.1039/C9NR01880H**.
10 L. S. Panchakarla, L. Lajaunie, A. Ramasubramaniam, R. Arenal and R. Tenne, *ACS Nano*, 2016, **10**, 6248–6256, DOI: **10.1021/acsnano.6b02430**.
11 L. S. Panchakarla, L. Lajaunie, A. Ramasubramaniam, R. Arenal and R. Tenne, *Chem. Mater.*, 2016, **28**, 9150–9157, DOI: **10.1021/acs.chemmater.6b04396**.
12 J. Lloyd, J. Clemens and R. Snede, *Microelectron. Reliab.*, 1999, **39**, 1595–1602, DOI: **10.1016/S0026-2714(99)00177-8**.
13 O. Hjortstam, P. Isberg, S. Söderholm and H. Dai, *Appl. Phys. A: Mater. Sci. Process.*, 2004, **78**, 1175–1179, DOI: **10.1007/s00339-003-2424-x**.
14 D. N. Futaba, K. Hata, T. Yamada, T. Hiraoka, Y. Hayamizu, Y. Kakudate, O. Tanaike, H. Hatori, M. Yumura and S. Iijima, *Nat. Mater.*, 2006, **5**, 987–994, DOI: **10.1038/nmat1782**.
15 J. R. Black, *IEEE Trans. Electron Devices*, 1969, **16**, 338–347, DOI: **10.1109/T-ED.1969.16754**.
16 M. Shatzkes and J. R. Lloyd, *J. Appl. Phys.*, 1986, **59**, 3890–3893, DOI: **10.1063/1.336731**.
17 C.-L. Liu, *Appl. Phys. Lett.*, 2002, **80**, 763–765, DOI: **10.1063/1.1445471**.
18 R. E. Hummel and H. J. Geier, *Thin Solid Films*, 1975, **25**, 335–342, DOI: **10.1016/0040-6090(75)90053-X**.
19 J. R. Lloyd, *J. Appl. Phys.*, 1991, **69**, 7601–7604, DOI: **10.1063/1.347529**.
20 P.-C. Li and T. K. Young, *IEEE Spectrum*, 1996, **33**, 75–78, DOI: **10.1109/6.535398**.
21 J. R. Lloyd and J. J. Clement, *Thin Solid Films*, 1995, **262**, 135–141, DOI: **10.1016/0040-6090(94)05806-7**.
22 W. H. Preece, *Proc. R. Soc. London*, 1883, **36**, 228–231, DOI: **10.1098/rspl.1883.0133**.
23 H. B. Huntington and A. R. Grone, *J. Phys. Chem. Solids*, 1961, **20**, 76–87, DOI: **10.1016/0022-3697(61)90138-X**.
24 J. Qin, P. Liao, M. Si, S. Gao, G. Qiu, J. Jian, Q. Wang, S. Zhang, S. Huang, A. Charnas, Y. Wang, M. J. Kim, W. Wu, X. Xu, H. Wang, L. Yang, Y. Yap and P. D. Ye, *Nat. Electron.*, 2020, **3**, 141–147, DOI: **10.1038/s41928-020-0365-4**.
25 A. Geremew, M. A. Bloodgood, E. Aytan, B. W. K. Woo, S. R. Corber, G. Liu, K. Bozhilov, T. T. Salguero, S. Rumyantsev, M. P. Rao and A. A. Balandin, *IEEE Electron Device Lett.*, 2018, **29**, 735, DOI: **10.1109/LED.2018.2820140**.

26 S. Song, S. Y. Kim, J. Kwak, Y. Jo, J. H. Kim, J. H. Lee, J. U. Lee, J. U. Kim, H. D. Yun, Y. Sim, J. Wang, D. H. Lee, S. H. Seok, T. il Kim, H. Cheong, Z. Lee and S. Y. Kwon, *Adv. Sci.*, 2019, **6**, 1801370, DOI: 10.1002/advs.201801370.
27 T. A. Empante, A. Martinez, M. Wurch, Y. Zhu, A. K. Geremew, K. Yamaguchi, M. Isarraraz, S. Rumyantsev, E. J. Reed, A. A. Balandin and L. Bartels, *Nano Lett.*, 2019, **19**, 4355–4361, DOI: 10.1021/acs.nanolett.9b00958.
28 S. Frank, P. Poncharal, Z. L. Wang and W. A. De Heer, *Science*, 1998, **280**, 1744–1746, DOI: 10.1126/science.280.5370.1744.
29 K. M. Mohsin and A. Srivastava, *IEEE Trans. Very Large Scale Integr. Syst.*, 2017, **25**, 3089–3098, DOI: 10.1109/TVLSI.2017.2737884.
30 K. Kaneto, M. Tsuruta, G. Sakai, W. Y. Cho and Y. Ando, *Synth. Met.*, 1999, **103**, 2543–2546, DOI: 10.1016/S0379-6779(98)00221-5.
31 R. Murali, Y. Yang, K. Brenner, T. Beck and J. D. Meindl, *Appl. Phys. Lett.*, 2009, **94**, 243114, DOI: 10.1063/1.3147183.
32 Z. Xu, Y. Liu, X. Zhao, L. Peng, H. Sun, Y. Xu, X. Ren, C. Jin, P. Xu, M. Wang and C. Gao, *Adv. Mater.*, 2016, **28**, 6449–6456, DOI: 10.1002/adma.201506426.
33 B. Q. Wei, R. Vajtai and P. M. Ajayan, *Appl. Phys. Lett.*, 2001, **79**, 1172–1174, DOI: 10.1063/1.1396632.
34 A. Naeemi and J. D. Mein, *IEEE Electron Device Lett.*, 2006, **27**, 338–340, DOI: 10.1109/LED.2006.873765.
35 Z. Yao, C. L. Kane and C. Dekker, *Phys. Rev. Lett.*, 2000, **84**, 2941, DOI: 10.1103/PhysRevLett.84.2941.
36 J.-W. Huang, C. Pan, S. Tran, B. Cheng, K. Watanabe, T. Taniguchi, C. N. Lau and M. Bockrath, *Nano Lett.*, 2015, **15**, 6836–6840, DOI: 10.1021/acs.nanolett.5b02716.
37 L. Dahéron, R. Dedryvère, H. Martinez, M. Ménétrier, C. Denage, C. Delmas and D. Gonbeau, *Chem. Mater.*, 2008, **20**, 583–590, DOI: 10.1021/cm702546s.
38 A. K. Opitz, C. Rameshan, M. Kubicek, G. M. Rupp, A. Nenning, T. Götsch, R. Blume, M. Hävecker, A. Knop-Gericke, G. Rupprechter, B. Klötzer and J. Fleig, *Top. Catal.*, 2018, **61**, 2129–2141, DOI: 10.1007/s11244-018-1068-1.
39 N. Domingo, E. Pach, K. Cordero-Edwards, V. Pérez-Dieste, C. Escudero and A. Verdaguer, *Phys. Chem. Chem. Phys.*, 2019, **21**, 4920–4930, DOI: 10.1039/C8CP07632D.
40 A. Hastir, R. L. Opila, N. Kohli, Z. Onuk, B. Yuan, K. Jones, Virpal and R. C. Singh, *J. Mater. Sci.*, 2017, **52**, 8502–8517, DOI: 10.1007/s10853-017-1059-9.
41 J.-H. Jhang, J. A. Boscoboinik and E. I. Altman, *J. Chem. Phys.*, 2020, **152**, 084705, DOI: 10.1063/1.5142621.
42 Z.-W. Gao, T. Ma, X.-M. Chen, H. Liu, L. Cui, S.-Z. Qiao, J. Yang and X.-W. Du, *Small*, 2018, **14**, 1800195, DOI: 10.1002/smll.201800195.
43 D. Barreca, A. Gasparotto, O. I. Lebedev, C. Maccato, A. Pozza, E. Tondello, S. Turner and G. Van Tendeloo, *CrystEngComm*, 2010, **12**, 2185, DOI: 10.1039/B926368N.
44 J. O. Hwang, D. H. Lee, J. Y. Kim, T. H. Han, B. H. Kim, M. Park, K. No and S. O. Kim, *J. Mater. Chem.*, 2011, **21**, 3432–3437, DOI: 10.1039/C0JM01495H.
45 A. S. Botana, P. M. Botta, C. de la Calle, A. Piñeiro, V. Pardo, J. Botana, M. Pereiro, D. Baldomir, J. A. Alonso and J. E. Arias, *J. Appl. Phys.*, 2011, **109**, 07E114, DOI: 10.1063/1.3536796.
46 A. Lekawa-Raus, J. Patmore, L. Kurzepa, J. Bulmer and K. Koziol, *Adv. Funct. Mater.*, 2014, **24**, 3661–3682, DOI: 10.1002/adfm.201303716.
47 Z. Lin, R. Zhan, L. Li, H. Liu, S. Jia, H. Chen, S. Tang, J. She, S. Deng, N. Xu and J. Chen, *RSC Adv.*, 2018, **8**, 2188–2195, DOI: 10.1039/C7RA11862G.
48 F. Urban, G. Lupina, A. Grillo, N. Martucciello and A. Di Bartolomeo, *Nano Express*, 2020, **1**, 010001, DOI: 10.1088/2632-959X/ab7055.
49 A. Al-Ghamdi, W. Boukhili and S. Wageh, *Synth. Met.*, 2021, **273**, 116670, DOI: 10.1016/j.synthmet.2020.116670.
50 R. Levi, O. Bitton, G. Leitus, R. Tenne and E. Joselevich, *Nano Lett.*, 2013, **13**, 3736–3741, DOI: 10.1021/nl401675k.
51 C. Florica, A. Costas, A. G. Boni, R. Negrea, L. Ion, N. Preda, L. Pintilie and I Enculescu, *Appl. Phys. Lett.*, 2015, **106**, 223501, DOI: 10.1063/1.4921914.
52 *Current carrying capacity*, No 24, 2010, Wellman Alloy Products.
53 J. Tao, N. W. Cheung and C. Hu, *IEEE Electron Device Lett.*, 1993, **14**, 249–251, DOI: 10.1109/55.215183.
54 J. R. Black, *Proc. IEEE*, 1969, **57**, 1587–1594, DOI: 10.1109/PROC.1969.7340.
55 C. Subramaniam, T. Yamada, K. Kobashi, A. Sekiguchi, D. N. Futaba, M. Yumura and K. Hata, *Nat. Commun.*, 2013, **4**, 2202, DOI: 10.1038/ncomms3202.
56 F. M. Brunbauer, E. Bertagnolli, J. Majer and A. Lugstein, *Nanotechnology*, 2016, **27**, 385704, DOI: 10.1088/0957-4484/27/38/385704.
57 W.-H. Xu, L. Wang, Z. Guo, X. Chen, J. Liu and X.-J. Huang, *ACS Nano*, 2015, **9**, 241–250, DOI: 10.1021/nn506583e.
58 M. L. Trouwborst, S. J. van der Molen and B. J. van Wees, *J. Appl. Phys.*, 2006, **99**, 114316, DOI: 10.1063/1.2203410.
59 M. F. Abdulhamid, C. Basaran and Y.-S. Lai, *IEEE Trans. Adv. Packag.*, 2009, **32**, 627–635, DOI: 10.1109/TADVP.2009.2018293.
60 M.-S. Yoon, M.-K. Ko, O.-H. Kim, Y.-B. Park, W. D. Nix and Y.-C. Joo, *J. Electron. Mater.*, 2007, **36**, 562–567, DOI: 10.1007/s11664-007-0102-z.
61 K. Zhao, T. Zhang, A. Ren, Y. Yang, P. Xiao, Z. Ge, Y. Ma and Y. Chen, *Carbon N. Y.*, 2019, **141**, 198–208, DOI: 10.1016/j.carbon.2018.09.040.
62 B. Han, E. Guo, X. Xue, Z. Zhao, L. Luo, H. Qu, T. Niu, Y. Xu and H. Hou, *Carbon N. Y.*, 2017, **123**, 593–604, DOI: 10.1016/j.carbon.2017.08.004.
63 M. A. Stolyarov, G. Liu, M. A. Bloodgood, E. Aytan, C. Jiang, R. Samnakay, T. T. Salguero, D. L. Nika, S. L. Rumyantsev, M. S. Shur, K. N. Bozhilov and A. A. Balandin, *Nanoscale*, 2016, **8**, 15774–15782, DOI: 10.1039/C6NR03469A.
64 O. V. Chernyj, G. F. Tikhinskij, G. E. Storozhilov, M. B. Lazareva, L. A. Kornienko, N. F. Andrievskaya, V. V. Slezov, V. V. Sagalovich, Y. D. Starodubov and S. I. Savchenko, *Supercond. Sci. Technol.*, 1991, **4**, 318–323, DOI: 10.1088/0953-2048/4/7/009.
65 Y. Peng and Q. Chen, *Nanoscale Res. Lett.*, 2012, **7**, 1–5, DOI: 10.1186/1556-276X-7-195.
66 A. R. Rathmell and B. J. Wiley, *Adv. Mater.*, 2011, **23**, 4798–4803, DOI: 10.1002/adma.201102284.

67 A. J. Molina-Mendoza, J. O. Island, W. S. Paz, J. M. Clamagirand, J. R. Ares, E. Flores, F. Leardini, C. Sánchez, N. Agraït, G. Rubio-Bollinger, H. S. J. van der Zant, I. J. Ferrer, J. J. Palacios and A. Castellanos-Gomez, *Adv. Funct. Mater*, 2017, **27**, 1605647, DOI: **10.1002/adfm.201605647**.

68 A. T. Neal, Y. Du, H. Liu and P. D. Ye, *ACS Nano*, 2014, **8**, 9137, DOI: **10.1021/nn5027164**.

69 K.-J. Lee, A. P. Chandrakasan and J. Kong, *IEEE Electron Device Lett.*, 2011, **32**, 557–559, DOI: **10.1109/LED.2011.2108259**.